remote sensing

MDPI

Article

Oil Spill Segmentation in Marine Radar Imager via an Enhanced GA-RBF-MBO Hybrid Approach

Jin Xu [1,2,3], Bo Xu [1,2], Jin Yan [1,2,3,*], Lihui Qian [4], Boxi Yao [1,2], Zekun Guo [1,2], Minghao Yan [1,2] and Peng Liu [5]

[1] Naval Architecture and Shipping College, Guangdong Ocean University, Zhanjiang 524091, China; jinxu@gdou.edu.cn (J.X.); xubo@stu.gdou.edu.cn (B.X.); yaoboxi@stu.gdou.edu.cn (B.Y.); zkguo@stu.gdou.edu.cn (Z.G.); yanmh@stu.gdou.edu.cn (M.Y.)
[2] Shenzhen Institute of Guangdong Ocean University, Shenzhen 518116, China
[3] Guangdong Provincial Key Laboratory of Intelligent Equipment for South China Sea Marine Ranching, Guangdong Ocean University, Zhanjiang 524088, China
[4] School of Computer Science, Huainan Normal University, Huainan 232038, China; cosmicflyer@hnnu.edu.cn
[5] Navigation College, Dalian Maritime University, Dalian 116026, China; liupeng@dlmu.edu.cn
* Correspondence: yanj@gdou.edu.cn; Tel.: +86-15842695866

Highlights

What is the main finding?

- An improved Monarch Butterfly Optimization (MBO) algorithm was proposed to achieve accurate identification and segmentation of oil spill regions from radar images.

What is the implications of the main finding?

- The improved MBO algorithm realized global threshold optimization, effectively suppressing clutter interference and obtaining higher accuracy and completeness in oil spill extraction.

Abstract

The continuous expansion of global maritime trade and shipping networks has increased the risk of marine oil spills. The increasing frequency of oil spill incidents has seriously threatened nearshore ecosystems, marine biological resources, and the sustainable development of coastal regions. An improved Monarch Butterfly Optimization (MBO) algorithm was proposed to achieve accurate identification and segmentation of oil spill regions in radar images. The original radar images underwent preprocessing, including grayscale conversion and background pixel removal, to preserve the informative pixels of oil films and improve the contrast between oil films and the seawater background. Subsequently, a genetic algorithm was employed to optimize the radial basis function (RBF) neural network, and a three-dimensional pixel feature space was constructed for oil spill Region of Interest (ROI) extraction. Finally, the improved MBO algorithm was applied to design a multi-objective fitness function integrating within-class variance, between-class differences, and class proportion constraints. Global optimization of the segmentation threshold was achieved via dynamic parameter adjustment, reverse learning, and elite reproduction, enabling accurate oil spill extraction. The precision, recall, F1 score, and IoU of the algorithm were 92.4%, 93.3%, 92.8%, and 86.6%, respectively. The proposed method achieves a well-balanced performance in both detection accuracy and region overlap, exhibits clear advantages over the compared methods in overall segmentation quality. The results demonstrated that the improved MBO algorithm mitigated segmentation challenges induced by low contrast and strong clutter, achieving superior classification accuracy and region completeness for offshore oil spill monitoring.

Check for updates

Academic Editors: Sen Lei, Liqin Liu and Zhengxia Zou

Received: 2 April 2026
Revised: 19 May 2026
Accepted: 25 May 2026
Published: 28 May 2026

Copyright: © 2026 by the authors. Licensee MDPI, Basel, Switzerland. This article is an open access article distributed under the terms and conditions of the Creative Commons Attribution (CC BY) license.

Keywords: oil spill; marine radar; GA-RBF; MBO

1. Introduction

Rapid growth in coastal oil terminal infrastructure has been accompanied by increasing port oil throughput and intensified maritime transportation activities [1]. As a result, the likelihood of oil spills has escalated markedly, presenting critical challenges to regional public safety, human health, economic stability, and coastal trade [2]. The energy demands of industrial production and societal development have driven the continuous maritime transport of substantial oil volumes to consumption centers [3]. During this process, accidents such as vessel collisions, groundings, and equipment failures can readily trigger sudden oil spills. Global annual oil discharge into the marine environment amounts to approximately 380 million gallons, driven by both natural factors, including extreme weather and oceanic conditions, and human factors such as operational errors [4,5]. This generates profound ecological degradation and exerts persistent pressures on the sustainable development of coastal regions.

Crude oil exhibits strong environmental persistence and degrades at a slow natural rate. Mineral oil discharged into the marine environment readily formed multilayer surface films that persisted on the sea surface for extended periods [6,7]. The formation of waxy oil layers on the sea surface substantially reduces sunlight penetration into the underlying water column, resulting in insufficient underwater illumination [8]. This process degrades marine water quality and exerts adverse effects on the marine ecosystem [9]. Existing studies have established a comprehensive framework addressing issues such as multilayered oil film formation, light attenuation, and marine water degradation [10]. This work provides a critical foundation for subsequent investigations.

Traditional machine learning and texture analysis methods are simple in structure and easy to implement. However, they generally exhibit high sensitivity to noise, limited feature representation, and insufficient adaptability to complex scenarios. Relevant studies have conducted a series of investigations integrating feature extraction with classical classifiers to address these challenges. Chen et al. implemented oil spill region extraction by combining image texture features with a BP neural network classifier and a thresholding method [11]. This approach achieved high recognition accuracy while preserving the completeness of oil film segmentation. Cheng et al. improved the noise sensitivity of the traditional K-means algorithm using inter-class separability metrics [12]. The enhanced algorithm was then combined with multi-source features to detect oil spill regions, achieving high detection rates. Xu et al. proposed an ocean oil spill detection approach that integrates Histogram of Oriented Gradients (HOG) features, a random forest (RF) classifier, and a particle swarm optimization (PSO) algorithm [13]. This method enables accurate and efficient detection of oil spill events, providing scientific support for offshore oil spill response. Li et al. focused on thermal infrared remote sensing images of oil spills and developed a detection scheme integrating Gray-Level Co-occurrence Matrix (GLCM) features with a Support Vector Machine (SVM) [14]. The scheme achieved a detection accuracy of 95% and demonstrated all-weather capability, enabling rapid and precise identification of various oil spill incidents.

Existing machine learning methods provided feasible solutions for SAR image interpretation. Nevertheless, their performance remains insufficient when handling complex SAR data, detecting small targets, and addressing imbalanced datasets. Deep learning, with its powerful feature extraction capabilities, has been widely adopted to overcome these limitations. Ma et al. constructed an intelligent oil spill detection model based on a deep convolutional neural network (DCNN) using dual-polarization data as input [15]. The

model integrates amplitude and phase features from the images, enabling precise identification and segmentation of small oil film regions. Prajapati et al. developed a GSCAT-UNET model for efficient oil spill detection and discrimination of similar targets [16]. The model significantly enhanced segmentation accuracy and robustness, addressing challenges posed by complex SAR data and imbalanced datasets. Sun et al. proposed the Multi-scale Attention Fusion U-shaped Transformer network (MAF-UFormer) [17]. By integrating multi-scale features with a surrogate attention mechanism, the model enhanced feature representation, and experimental results demonstrated its significant advantages in oil spill detection tasks. Bianchi et al. developed a deep learning framework for large-scale detection and classification of oil spills in synthetic SAR images [18]. After extensive training on large datasets, the neural network segmentation model demonstrated excellent performance in oil spill detection tasks. Cai et al. proposed a detection method tailored for few-shot scenarios, developing a single-image generative adversarial network (SinGAN) capable of training from a single oil spill image [19]. The method further applied transfer learning to train the YOLO-V8 model, achieving superior performance across multiple metrics in oil spill detection. Zhang et al. developed a lightweight DeepLabV3+ model that utilized MobileNetV2 to reduce computational complexity and integrated a spatial-channel squeeze-and-excitation module for enhanced feature representation [20]. The model employed a combined BCE-Dice loss function, effectively enhancing the capture of fine-grained features in oil spill regions. Lau et al. applied a U-Net combined with a mask-based convolutional neural network for nearshore in situ oil spill detection, integrating geographic information systems (GIS) to enhance deep model performance [21]. Experimental results demonstrated that this approach significantly improved the efficiency of traditional oil spill detection methods.

Single deep learning models often underutilize dedicated sensors and multi-source remote sensing data, limiting their ability to cover diverse observation scenarios. Nevertheless, deep learning methods have demonstrated strong capability in automatic feature extraction and complex pattern representation, enabling improved discrimination between oil spill regions and surrounding sea clutter. In addition, advanced network architectures can effectively capture multi-scale spatial information, which contributes to enhanced detection accuracy and robustness under complicated marine environments. Wang et al. proposed a marine oil spill detection method based on a Monte Carlo-based deep Q-transfer-learning network (DQTN) [22]. Remote sensing data were employed to detect marine oil spill events, while an offline transfer deep Q-network was further utilized to determine the locations of oil spill sources. Accurate monitoring of oil spill locations was thereby achieved. Li et al. proposed a novel self-evolving automatic oil spill monitoring algorithm that integrated three interconnected modules, including oil spill detection, new training data generation, and deep learning model enhancement [23]. Through self-evolving training cycles and continuous generation of new training data, the parameters of the deep learning model were automatically updated, thereby continuously improving the accuracy of oil spill detection. Yuan et al. proposed a sea surface oil spill detection method based on differential-polarization FTIR spectroscopy [24]. Experimental results demonstrated that this approach effectively identified oil pollutants in water, addressing the limitations of traditional thermal remote sensing techniques in detecting surface oil spills. Iordache et al. employed a lightweight ultraviolet (UV) camera to investigate the potential of UV imaging for oil spill detection and conducted simulated experiments under various environmental conditions [25]. Experimental results indicated that UV imaging outperformed RGB imaging in detecting oil spills. Chen et al. introduced a deep learning-based oil spill detection method that utilizes Sentinel-1 PolSAR satellite imagery to identify oil pollutants on the ocean surface [26]. By integrating polarization measurements and wind speed data, this

approach significantly enhanced the accuracy of oil spill detection. Liu et al. presented a texture-based detection method using X-band marine radar imagery [27]. Accurate extraction of oil spill regions was achieved by applying adaptive thresholding within candidate areas defined by the constructed texture indices. Rousso et al. enhanced the physical characteristics and visual appearance of oil spills using SAR image filtering techniques [28]. Precision extraction of oil spill regions was achieved by employing geometric modeling to reduce generalization errors.

Current methods primarily focus on static detection and exhibit limitations in dynamic tracking, rapid emergency response, and unsupervised efficient identification. Consequently, integrated detection approaches targeting real-time operation, dynamic evolution, and high-efficiency decision-making have been developed. Karantzalos et al. applied a level-set–based image segmentation method to search-and-rescue imagery to achieve real-time detection and tracking of oil spills [29]. Experimental results demonstrated that the level-set segmentation effectively identified oil spills and performed robustly under sudden spill scenarios. Liu et al. leveraged the potential of change detection (CD) techniques to develop an unsupervised, semi-automatic, and efficient method for oil spill identification [30]. A coarse-to-fine multi-temporal change analysis workflow was designed, providing an effective solution for rapid oil spill detection and demonstrating its validity in real spill events. Lyu et al. designed a hybrid modeling approach integrating deep learning with numerical simulation [31]. The method employs a diffusion LSTM to extract temporal features and leverages simulated trajectories to generate short-interval oil spill scene images, thereby enhancing detection efficiency. Tan et al. proposed an intelligent approach for the automated identification and quantitative analysis of GC/MS spectra [32]. Leveraging the associated database, the method enables rapid determination of oil sample diagnostics and identification of suspicious oils within minutes, thereby enhancing oil spill detection efficiency.

In summary, marine oil spills pose a serious threat to nearshore ecosystems and the long-term sustainability of coastal regions. Accurate oil spill identification and segmentation in marine radar imagery remain highly challenging. This difficulty mainly arises from the low contrast between oil films and seawater, as well as the strong interference caused by complex sea clutter. Existing optimization-based segmentation approaches often exhibit unstable convergence behavior, insufficient regional consistency, and excessive false-positive responses under such environmental conditions. In addition, many contemporary deep learning approaches rely heavily on large-scale annotated datasets and extensive training procedures. This limitation restricts their applicability in practical marine monitoring scenarios with limited labeled samples.

Against this background, a deterministic optimization-based segmentation framework founded on an improved Monarch Butterfly Optimization (MBO) algorithm is developed for robust marine oil spill extraction. Unlike conventional data-driven learning paradigms, the proposed framework achieves stable segmentation performance without dependence on large-scale training datasets. This characteristic improves its applicability and practicality in low-annotation marine environments. The principal methodological contributions of this study can be summarized as follows:

(1) A deterministic segmentation framework is established for oil spill extraction in low-contrast marine environments. The framework enables stable and reliable segmentation performance while avoiding reliance on data-driven learning models.

(2) Dynamic parameter adaptation is incorporated into the optimization process. This strategy enhances convergence stability and environmental adaptability under complex marine clutter conditions. As a result, the robustness of the segmentation framework is significantly improved.

(3) An opposition-based learning mechanism is embedded within the optimization framework. The mechanism strengthens population diversity and global exploration capability. It also alleviates the premature convergence problem commonly encountered in conventional MBO optimization.

(4) An elite reproduction strategy is introduced to reinforce local exploitation capability and convergence refinement. This design leads to more stable optimization behavior and more accurate oil spill boundary delineation.

(5) A multi-objective fitness optimization framework is constructed by jointly integrating inter-class separability, intra-class consistency, and edge structure characteristics. This design significantly improves the discrimination capability between oil spill regions and complex marine background clutter.

Through the synergistic interaction of these strategies, the proposed framework substantially enhances the separability between oil spill regions and surrounding clutter. Meanwhile, false detections and missed detections are effectively suppressed. Experimental results further demonstrate that the proposed method achieves superior segmentation accuracy, regional consistency, and robustness compared with existing optimization-based segmentation approaches. These advantages indicate that the proposed framework provides an efficient and practical solution for maritime oil spill monitoring applications.

2. Experimental Data and Methods

2.1. Experimental Data

The radar image data used in this experiment were collected at sea by the teaching-training ship *Yukun* of Dalian Maritime University. The data acquisition tasks were divided into routine navigation and targeted oil spill observation, both based on actual oil spill scenarios occurring near the Dalian Bay port area, as shown in Figure 1a. The core device used for data acquisition in the experiment was an X-band radar with detection capability, as shown in Figure 1b. Its effective detection range reached 0.75 nautical miles. The experimental dataset consisted of raw shipborne radar images with a resolution of 1024 × 1024 pixels. The system continuously sampled the sea surface at two-second intervals to capture the dynamic changes in the sea surface. This acquisition approach preserved the spatial resolution of the data while demonstrating the practical effectiveness of the X-band radar in real-world conditions. The experimental platform is equipped with a 12th Gen Intel(R) Core(TM) i5-12400F processor (2.50 GHz), 16.0 GB memory, and an NVIDIA GeForce GTX 1660 SUPER (6 GB) GPU. Under this configuration, the proposed improved MBO algorithm requires an average processing time of 3.26 s for a single radar image. The computational complexity of the algorithm is $O(T \cdot N \cdot M)$, where T denotes the maximum number of iterations, N is the population size, and M represents the number of valid pixels.

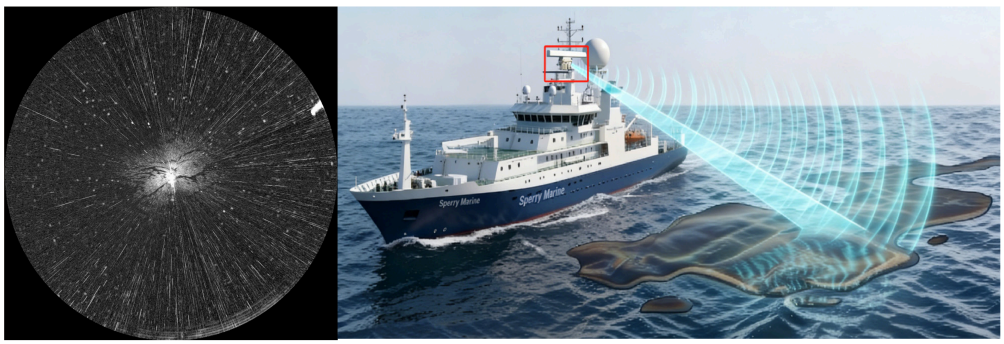

(**a**) (**b**)

Figure 1. Experimental data. (**a**) Raw radar data and (**b**) Data acquisition platform. The X-band radar antenna is indicated within the red box.

2.2. Experimental Flow

The overall procedure for the precise detection of oil spill regions in marine radar images used here is shown in Figure 2. First, standardized preprocessing was performed on the collected raw marine radar data. The problems of low signal-to-noise ratio and insufficient target detection in the raw data were addressed. This provided high-quality and highly consistent image input for subsequent processing. Subsequently, the Genetic Algorithm-Radial Basis Function (GA-RBF) model was applied to perform target localization based on the preprocessing results. The Region of Interest (ROI) containing oil spill candidate regions was accurately extracted, and pure background redundant regions were effectively removed. The target features were fully preserved, and the computational cost and background clutter interference in the subsequent segmentation stage were significantly reduced. Finally, the improved MBO algorithm was applied to perform adaptive threshold segmentation on the extracted oil spill ROI image. Oil spill targets were accurately separated from background pixels, resulting in segmentation outputs with precise boundaries and complete structural details.

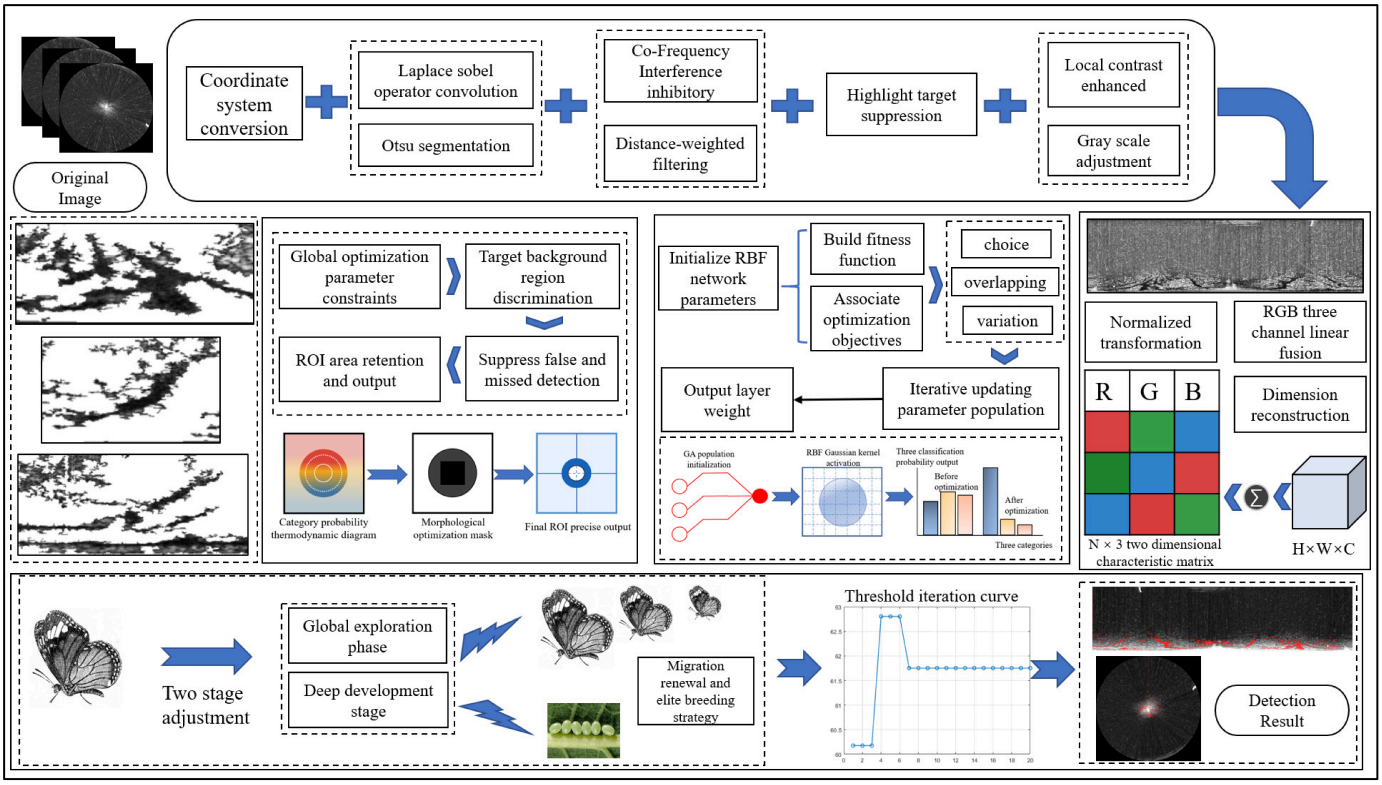

Figure 2. Experimental Flowchart.

2.3. Pre-Processing Data

First, the original marine radar image was transformed from polar coordinates to Cartesian coordinates. This established a unified spatial reference framework and provided the basis for subsequent pixel-level processing. Thereafter, the Laplacian operator convolution and the Otsu threshold segmentation method were combined to preliminarily suppress co-frequency interference noise. Then, the adaptive distance-weighted filtering algorithm was applied to further improve the denoising performance for co-frequency interference. Next, the overall gray-level distribution was further optimized and adjusted, enabling precise identification and effective suppression of speckle noise, and global gray-level normalization was simultaneously completed. Ultimately, a local contrast enhancement strategy was applied. The gray-level differences between the interior and exterior of the

oil film region and between the oil film and the wave background were enhanced, thereby improving the distinguishability of the target region.

2.4. ROI Extraction Using GA-RBF

(a) Image data processing and feature space mapping.

The GA was employed to optimize the center and width parameters of the RBF neural network, enabling the construction of an intelligent model for three-class image classification. The GA was employed to optimize the center and width parameters of the RBF neural network. The global random seed was set to 1. The optimization variable dimension was set to 16, the population size was set to 15, and the crossover probability was set to 0.8. A single-point crossover strategy, uniform selection method, and adaptive feasible mutation method were adopted. The optimal network structure was automatically identified via the genetic algorithm, overcoming the difficulty of determining traditional RBF parameters [33,34]. The original spatial structure images were subsequently transformed into feature representations suitable for neural network processing. Since low-precision integer image formats may introduce precision loss and numerical overflow during nonlinear operations and matrix computations, normalization processing was performed to maintain feature consistency and computational stability. In addition, data type promotion and dimensional reconstruction were conducted to improve numerical robustness and provide a reliable foundation for subsequent feature extraction and parameter optimization.

Through dimensional reconstruction, the three-dimensional image data were converted into a two-dimensional pixel feature matrix. A training sample set was then constructed using a random uniform sampling strategy, where B_i represents the brightness feature value of the i-th training sample:

$$B_i = \sum_{c=1}^{3} X_t(i,c) + \varepsilon \cdot \mathrm{randn}(1) \tag{1}$$

$$X_t = \Gamma(\mathrm{vec}(\mathrm{double}(I(x,y,c))), M) \tag{2}$$

where c is the channel index, ε is the minor disturbance coefficient, which is taken as 10^{-6} in this experiment to avoid sorting ambiguity caused by identical brightness values. $\mathrm{randn}(1)$ is the standard normal distribution random number generation operator, X_t is the training sample feature matrix, $\Gamma(\cdot)$ is a random uniform sampling operator, $\mathrm{vec}(\cdot)$ is the vectorized operator, $\mathrm{double}(\cdot)$ is a data type conversion operator that converts pixel values to double-precision floating-point type. $I(x,y,c)$ is the pixel value of the original image, (x,y) is the pixel spatial coordinate, M is the number of training samples.

(b) Three class label constructions based on brightness features.

The brightness features were first sorted in ascending order and divided using equal-frequency interval partitioning. Training samples were then categorized into three distinct classes, namely low, medium, and high. This strategy ensured that the classification results remained highly consistent with the actual visual characteristics of the image pixels and avoided class confusion and learning bias caused by random partitioning. An equal-proportion partitioning strategy was subsequently adopted to ensure a balanced number of samples across the three categories. This approach effectively suppressed the bias introduced by class imbalance during model training.

The discrete class labels were converted into one-hot encoded representations to ensure compatibility with the multi-output architecture of the RBF neural network. It also guaranteed that the loss function computation, gradient backpropagation, and parameter

update processes strictly adhered to the optimization logic of multi-class tasks. $Y_t(i,k)$ is the unique encoding value of the k-th class corresponding to the i-th training sample:

$$Y_t(i,k) = \begin{cases} 1,\ \Pi(i) \in \left[\lfloor \frac{M}{3} \rfloor (k-1)+1,\quad \lfloor \frac{M}{3} \rfloor k\right] \\ 0,\ \text{otherwise} \end{cases} \tag{3}$$

$$\Pi = \text{argsort}(B + \delta \cdot \text{rand}(M,1)) \tag{4}$$

$$B = \left[B_1, B_2, \ldots, B_M\right]^T \tag{5}$$

where k is the category index, with values 1, 2, and 3 corresponding to low brightness, medium brightness, and high brightness categories, respectively. $\lfloor \cdot \rfloor$ is the down rounding operator used for equal frequency partitioning of three types of samples, Π is the brightness feature ranking index vector, $\text{argsort}(\cdot)$ is the sorting index operator that outputs the index sequence of the original sample. $\text{rand}(M,1)$ is the operator for generating uniformly distributed random numbers, B is the training sample brightness feature vector.

(c) Genetic Algorithm Optimization of RBF Neural Network.

The nonlinear mapping capability, feature fitting accuracy, and classification performance of the RBF neural network strongly depended on the hidden layer center vectors and the proper configuration of the Gaussian kernel widths. Traditional parameter initialization methods could only achieve local optimization of hidden layer centers and could not perform joint optimization of the center vectors and kernel widths. The GA was employed for global parameter optimization, where the population was iteratively evolved within a predefined parameter space through selection, crossover, and mutation operations. In this study, the GA was used to optimize the hidden layer center vectors and Gaussian kernel width parameters of the RBF neural network. The fitness function was formulated based on the mean squared error calculated from the training samples. The GA-based parameter optimization strategy effectively avoided local optima and improved the fitting capability of the model for nonlinear pixel features.

During the output layer weight determination process, the output weight matrix was analytically solved using regularized least squares once the hidden layer centers and kernel width parameters were determined. A small regularization term was introduced to suppress singularity in the hidden layer output matrix and improve numerical stability during weight calculation. The parameter vector v represents the hidden layer center vectors and Gaussian kernel width parameters optimized through GA optimization. The $W(v)$ is the output weight matrix determined by the regularized least-squares method under the parameter vector v:

$$v = [C_1, C_2, \ldots, C_k, \sigma] \tag{6}$$

$$v^* = \underset{v\in\Omega}{\text{arg}min} \frac{1}{M} \sum_{i=1}^{M} \parallel Y_t(i,:) - \Phi(i,:)W(v) \parallel_2^2 \tag{7}$$

$$\Phi_{v,ij} = \exp\left(-\frac{\parallel X_t(i,:) - \boldsymbol{c}_j \parallel_2^2}{2\sigma^2 + \tau}\right) \tag{8}$$

$$W(v) = \left(\Phi_v^T \Phi_v + \lambda I_K\right)^{-1} \Phi_v^T Y_t \tag{9}$$

where C_j represents the center vector of the j-th RBF hidden layer node, σ is the Gaussian kernel width parameter. $\underset{v\in\Omega}{\text{arg}min}$ is a constrained minimum value solving operator, Ω is the parameter constraint space, $\Phi(i,:)$ is the i-th row of the hidden layer output matrix Φ, which is the output of all hidden layer neurons for the i-th sample. $\| \cdot \|_2^2$ is the square of the

Euclidean distance, which calculates the spatial distance between the training sample and the center of the hidden layer. Φ_{ij} is the output value of the Gaussian kernel function at the center of the jth hidden layer of the ith training sample in the RBF neural network. $\exp(\cdot)$ is a natural exponential function that characterizes the similarity between the sample and the center of the hidden layer, $X_t(i,:)$ is the i-th row of the training sample feature matrix X_t, which is the RGB three-channel feature vector of the i-th training sample. τ is a minor disturbance term, which is taken as 10^{-7} in this experiment to improve the stability of the formula. λ is the regularization coefficient, with a value of 10^{-5} in this experiment, to ensure stable weight calculation, I_K is a k-order identity matrix, and a regularization term is constructed to avoid overfitting.

(d) Whole image pixel classification and ROI extraction.

Full image pixel features were fed into the optimized network model, and pixel-wise classification results were subsequently obtained. The optimal model performance achieved during training was further generalized to the entire image, ensuring the consistency, accuracy, and reliability of the full-image classification results. A category filtering threshold was defined to achieve a preliminary separation between the target class and the background class. An initial binary mask was generated, after which the refined mask was fused with the preprocessed image using pixel-wise weighted fusion. This operation preserved the color characteristics of the target region and performed value calibration on the image. Consequently, precise ROI extraction, enhancement, and visualization were achieved. $I_r(x,y,c)$ is the pixel value of the (x, y)-th pixel and the c-th channel in the final ROI image:

$$I_r(x,y,c) = \text{closerect}(M_{\text{init}}(x,y),\gamma)\cdot I(x,y,c) + 255\cdot(1 - \text{closerect}(M_{\text{init}}(x,y),\gamma)) \quad (10)$$

$$M_{\text{init}}(x,y) = \begin{cases} 1, C(x,y) = 1 \\ 0, otherwise \end{cases} \quad (11)$$

$$\mathbf{C}(x,y) = \text{argmax}\left(\exp\left(-\frac{||X_f((x-1)W+y,:) - \boldsymbol{c}_j^*(\boldsymbol{v}^*)||_2^2}{2\sigma^*(\boldsymbol{v}^*)^2 + \tau}\right)W^*(v^*)\right)_k \quad (12)$$

where $\text{closerect}(\cdot,\gamma)$ is the morphological closed operator, γ is the size of the closed operation rectangular window, $M_{\text{init}}(x,y)$ is the initial binary mask, $C(x,y)$ is the classification result of the (x, y)-th pixel in the image. $X_f((x-1)W+y,:)$ is the corresponding row of the pixel feature matrix X_f for the entire image, $\boldsymbol{c}_j^*$ is the optimal hidden layer center vector.

2.5. Improved MBO Algorithm for Extracting Oil Spill Targets

(a) Effective pixel extraction and adaptive initialization of algorithm parameters.

An improved MBO algorithm was employed to simulate butterfly migration and mating behaviors, enabling adaptive global search for the image segmentation threshold. Migration updating, reverse learning, and elite reproduction mechanisms facilitated efficient convergence toward the optimal threshold during iteration [35–37]. The improved MBO stage was applied within the extracted ROI rather than the entire radar image, thereby reducing background interference and improving fine-scale segmentation accuracy. The grayscale values of background regions were typically stable and contained little useful information, whereas oil spill regions generally exhibited lower grayscale values. The accuracy of threshold optimization was improved by performing effective region screening on the ROI image. Irrelevant background pixels were removed by using a grayscale threshold, while only the valid pixel regions containing oil spill targets and seawater information were retained. The grayscale statistical distribution characteristics of the valid pixels were subsequently analyzed together with the pixel dispersion and value range. This process

enabled adaptive matching between the algorithm parameters and the characteristics of the image data.

This step enhanced the specificity of the threshold search and improved the integrity and reliability of the subsequent segmentation results. This strategy provided reliable support for subsequent fitness evaluation and alleviated dependence on manual parameter adjustment in the traditional MBO algorithm. $M(x, y)$ is the effective pixel mask matrix:

$$M(x,y) = \begin{cases} 1, I_r(x,y,c) \neq 255 \\ 0, otherwise \end{cases} \tag{13}$$

$$N = \text{round}\left(k_1 + \frac{\sigma_P}{k_2}\right) \tag{14}$$

$$[L, U] = [min(P) - \delta, max(P) + \delta] \tag{15}$$

where N is the population size of the MBO algorithm, k_1, k_2 is a constant coefficient used to adaptively adjust the population size, σ_P is the gray standard deviation of the effective pixel set. $[L, U]$ is the adaptive search interval of the segmentation threshold, P denotes the set of valid pixels, corresponding to the elements where $M(x, y) = 1$, δ is the interval expansion coefficient.

(b) Two-stage dynamic parameter adaptive adjustment.

The traditional MBO algorithm exhibited limitations in balancing global exploration with the prevention of premature convergence and entrapment in local optima. Consequently, the iterative process was divided into a global exploration phase and a deep exploitation phase. Different parameter control strategies were adopted for different optimization stages to improve convergence stability and search adaptability. The iteration number was preset as the phase transition criterion. During the early optimization stage, larger migration step sizes were employed to enhance global exploration capability and maintain population diversity. In the later optimization stage, the migration step size was gradually reduced while the elite reproduction probability was increased to strengthen local exploitation capability and convergence refinement. The iteration number was preset as a dividing point, and different stages employed differentiated parameter control strategies. The iteration progress factor was used to achieve a continuous and smooth transition of the migration step size and elite reproduction probability. This enabled the algorithm to possess targeted search capabilities during different optimization cycles.

The improved MBO algorithm maintained strong global traversal capability during the exploration phase through dynamic parameter adjustment. During the exploitation phase, local fine-grained search was progressively strengthened, and the elite reproduction probability was increased. $f(t)$ is the adaptive migration step size of the t-generation. $SR(t)$ is the elite reproductive probability of the t-generation:

$$f(t) = \frac{\mathrm{U} - \mathrm{L}}{\mathrm{N}} \cdot (f_{max} - (f_{max} - f_{min}) \cdot \frac{t - G_c}{T_{max} - G_c}) \tag{16}$$

$$SR(t) = \left(1 - \frac{1}{\mathrm{N}}\right) \cdot SR_{min} + (SR_{max} - SR_{min}) \cdot \frac{t - G_c}{T_{max} - G_c} \tag{17}$$

where f_{max} is the upper limit of the exploration stage step size, f_{min} is the lower limit of the development stage step size. SR_{max} is the upper limit of the development phase, SR_{min} is the lower limit of the exploration stage. t is the current iteration count, G_c is the stage switching algebra, which is used to divide the global exploration stage and the local exploitation stage. In this experiment, it is set to a fixed value of 10. T_{max} is the maximum number of iterations for the algorithm.

(c) Individual update strategy integrating migration and reverse learning.

An opposition-based learning strategy and boundary constraint mechanism were introduced. These measures expanded population diversity and the effective search space, thereby enhancing the capability of the algorithm to escape local optima. Each individual in the population was first guided toward the current global best solution using the migration operator. Adaptive migration step sizes and random perturbations were then used to generate new candidate positions.

A symmetric opposition solution was constructed based on the migrated position. This operation enlarged the search range and strengthened the global exploration capability. The boundary constraint mechanism was applied after position updating to ensure the feasibility of candidate solutions. In this way, the modified update strategy maintained the convergence trend toward high-quality solutions while improving the ability to escape premature convergence. $X_i^m(\mathrm{t})$ is the updated candidate position of the i-th monarch butterfly in the t-generation migration:

$$X_i^m(\mathrm{t}) = X_i(t) + f(t) \cdot r_1 \cdot (X_{\mathrm{best}}(t) - X_i(t)) \tag{18}$$

$$X_i^r = L + U - X_i^m(\mathrm{t}) \tag{19}$$

where $X_i(t)$ is the current position of the i-th monarch butterfly individual in the t-generation, r_1 is a random number within [0, 1], used to increase search randomness. $X_{\mathrm{best}}(t)$ is the global optimal position of the entire population of the t-generation monarch butterfly, X_i^r is a reverse learning candidate position generated based on the migration location of the i-th monarch butterfly individual.

(d) Elite guided reproduction and greedy retention strategy.

A subset of individuals with higher fitness values in the population was selected here to form an elite set, which served as a high-quality gene pool. Through the elite crossover mechanism, candidate solutions were recombined with randomly selected elite solutions to generate offspring positions, thereby facilitating the propagation of advantageous solution information within the population. During the individual update process, a greedy selection mechanism was employed. Replacement was performed only when the fitness of the newly generated reproduction position exceeded that of the original individual. This strategy ensured the continuous improvement of population quality while reducing the influence of inferior candidate solutions on the optimization process.

The elite-guided reproduction strategy effectively accelerated population convergence and improved local exploitation capability during the later optimization stage. The greedy update mechanism strictly selected high-quality solutions, avoided low-quality solutions from interfering with the optimization direction, and ensured algorithm stability:

$$X_i(t+1) = \begin{cases} X_i^*(t) + r_2 \cdot \left(X_e(t) - X_i^*(t)\right) \; F\left(X_i^*(t) + r_2 \cdot \left(X_e(t) - X_i^*\right)\right) < F(X_i(t)) \\ X_i(t) \; F\left(X_i^*(t) + r_2 \cdot \left(X_e(t) - X_i^*(t)\right)\right) \geq F(X_i(t)) \end{cases} \tag{20}$$

where $X_i^*(t)$ is the candidate position obtained by the monarch butterfly after migration, reverse learning, and selection. $X_e(\mathrm{t})$ is a randomly selected parent elite individual from the elite set. $F(\cdot)$ is the fitness function used to evaluate the quality of segmentation thresholds.

(e) Multi-dimensional weighted fitness function for oil spill segmentation.

The fitness function of the traditional MBO algorithm relied on a single evaluation metric. This made it difficult to satisfy the comprehensive requirements of marine oil spill segmentation. Therefore, a multi-dimensional weighted fitness function integrating intra-class variance, inter-class variance, and area balance constraints was constructed. It quantitatively evaluated the segmentation threshold from multiple key dimensions of

segmentation quality. This transformed the multi-objective optimization problem into a single optimizable objective. It thereby improves the discrimination capability between oil spill regions and background clutter.

This transformed the multi-objective optimization problem into a single optimizable objective. It thereby improves the discrimination capability between oil spill regions and background clutter. $F(T)$ is the fitness value corresponding to the segmentation threshold T:

$$F(T) = w_1 \cdot \left(\sigma_f^2 + \sigma_b^2\right) + w_2 \cdot \frac{1}{(\mu_f - \mu_b)^2 + \varepsilon} + w_3 \cdot \left(\frac{N_f}{N_P} - c\right)^2 \tag{21}$$

where σ_f^2, σ_b^2 represents the intra-class variance of foreground and background pixels, respectively. μ_f, μ_b represents the grayscale values of foreground and background pixels, respectively, N_f, N_P represents the number of foreground pixels and the total number of image pixels, respectively. w_1, w_2, w_3 are weighting coefficients for evaluation indicators to ensure numerical stability. c is the area balance coefficient, which is taken as 0.5 in this experiment.

(f) Optimal threshold decision and oil spill area segmentation.

When the algorithm reached the maximum number of iterations, the optimization process was terminated, and the final global optimal individual position was mapped to the optimal segmentation threshold. Subsequently, the optimal threshold was used to perform binary segmentation on the effective pixel regions. Oil spill regions and the seawater background were distinguished based on the relationship between pixel gray values and the threshold, yielding the initial segmentation result of the oil spill regions.

The improved MBO algorithm obtained the optimal threshold through global search. It exhibited stronger objectivity, stability, and adaptability, making it suitable for oil spill images in different scenarios. $O'(x, y)$ is the final oil spill segmentation result:

$$O'(x, y) = \text{Post}\left(\begin{cases} 1, M(x, y) = 1,\ I_r(x, y, c) < X_{best}^{T_{max}}(t) \\ 0, \text{ otherwises} \end{cases}\right) \tag{22}$$

where $X_{best}^{T_{max}}(t)$ is the global optimal position at the end of the iteration, which is the optimal segmentation threshold, $M(x, y)$ is the effective pixel mask matrix, $\text{Post}(\cdot)$ is the morphological post-processing operator.

3. Results

3.1. Preprocessing Result

Experimental results showed that the preprocessed image was standardized via spatial coordinate mapping and corrected the geometric distortions present in the original polar coordinate data. The gray-level difference between oil spill regions and the sea wave background was significantly increased, which effectively improved the distinguishability of weak-reflection oil spill targets. The final preprocessing result is shown in Figure 3.

3.2. ROI Extraction

The method used in this experiment effectively distinguished target regions from background regions. High classification consistency and regional integrity were maintained under complex pixel distribution conditions, as shown in Figure 4a. The combined effect of the Gaussian kernel function and global optimization parameters enabled the model to accurately capture pixel feature differences across different brightness ranges. Misclassification and missed detection caused by local optima were avoided. Finally, ROI regions

encapsulating salient target information were preserved, thereby suppressing redundant interference, as shown in Figure 4b.

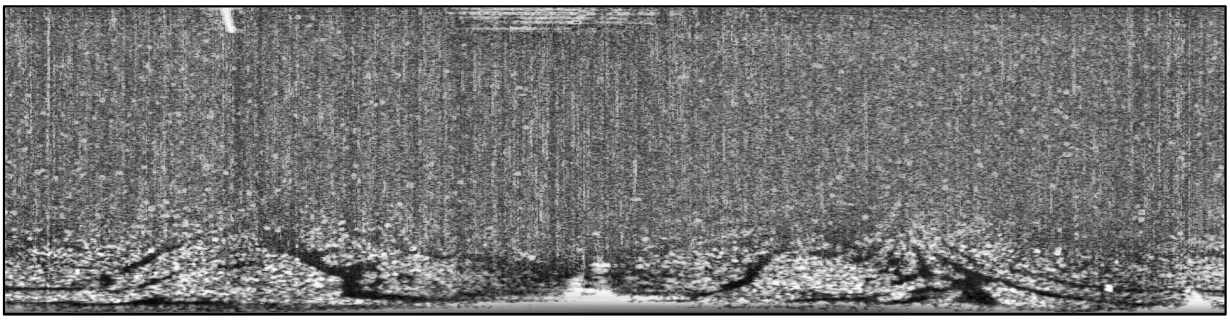

Figure 3. Preprocessing result image.

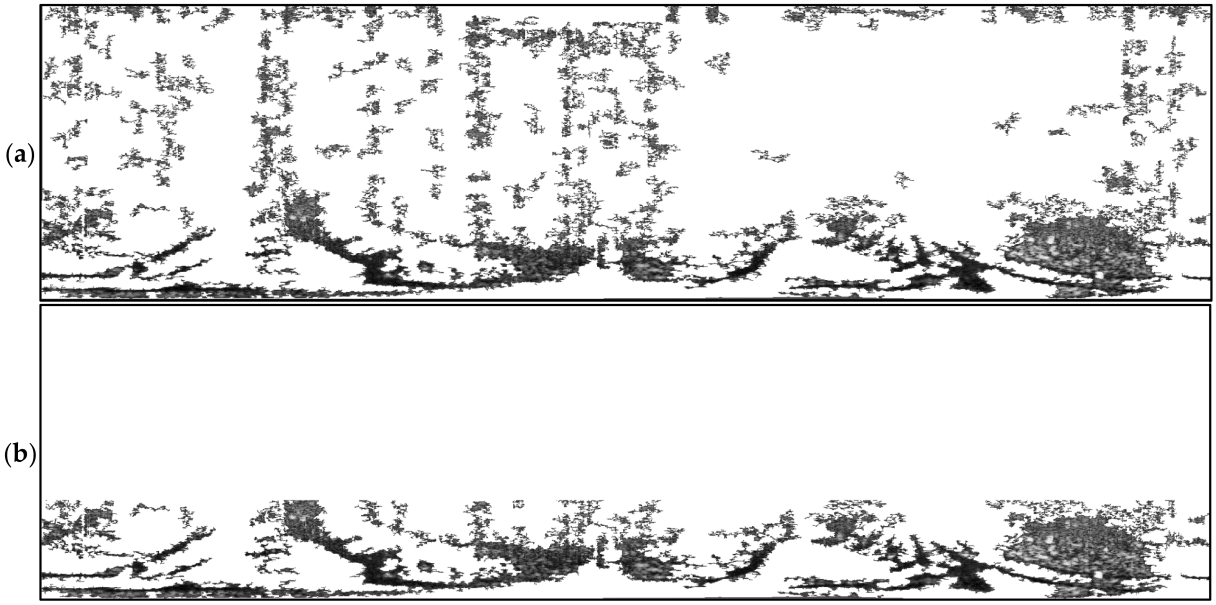

Figure 4. Oil spill interest area extraction result: (**a**) Extraction map of complete oil spill interest area and (**b**) ROI map of interference removal area.

3.3. Image Segmentation Results of Improved MBO Algorithm

The improved MBO algorithm achieved more stable and accurate segmentation results in marine radar imagery. The red masked regions in Figure 5 represent the oil spill areas identified by the proposed method. Compared with conventional optimization approaches, the improved MBO algorithm obtained better fitness convergence performance and reached a stable state within fewer iterations. It achieved higher segmentation accuracy and a better fitness convergence value, and reached a stable convergence state within fewer iterations. This provided a more reliable segmentation basis for marine oil spill monitoring.

The segmentation results indicate that the proposed method effectively enhanced the discrimination capability between oil spill regions and surrounding clutter. More complete oil spill boundaries and improved regional consistency were also achieved during the segmentation process, providing reliable support for marine oil spill monitoring.

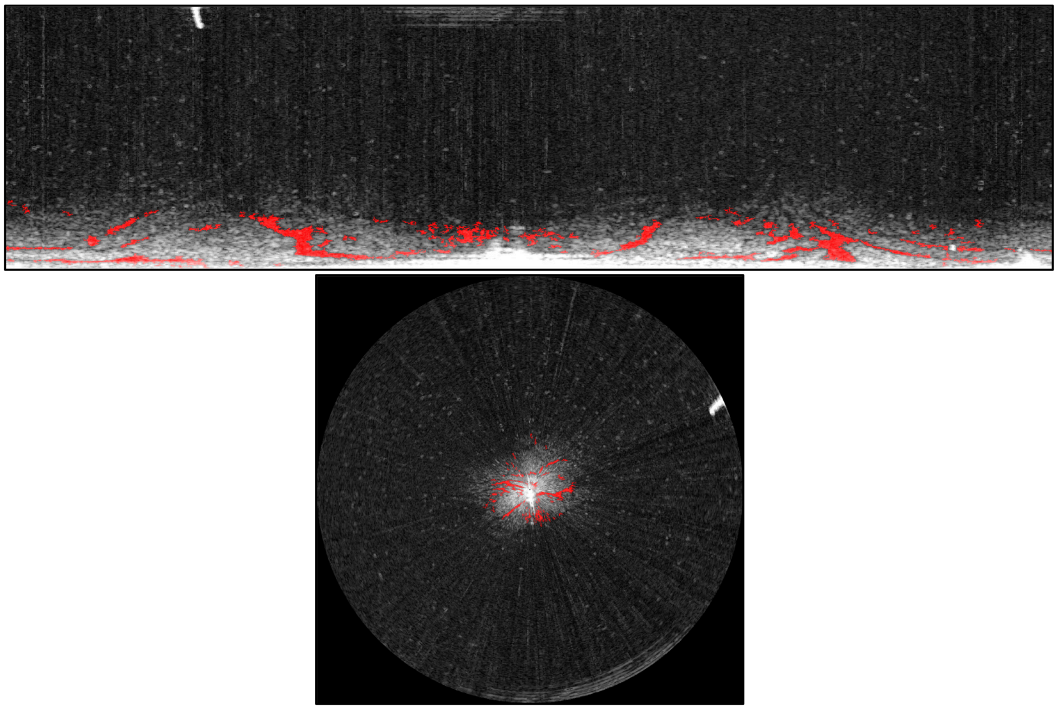

Figure 5. Oil film marking image: (**a**) Oil film marking image in polar coordinates and (**b**) Image of oil film marker in Cartesian coordinate system.

4. Discussion

4.1. Comparison with Traditional MBO Algorithm

The effectiveness of the improved MBO algorithm in oil spill segmentation was validated through comparison with the traditional MBO algorithm. The traditional MBO algorithm employed fixed parameter settings and updated the population through simple migration and random walk mechanisms. It lacked adaptability to oil spill segmentation scenarios. In addition, its single fitness function failed to simultaneously ensure segmentation accuracy and the integrity of oil spill regions. The oil film detection result obtained by using the traditional MBO algorithm is shown in Figure 6.

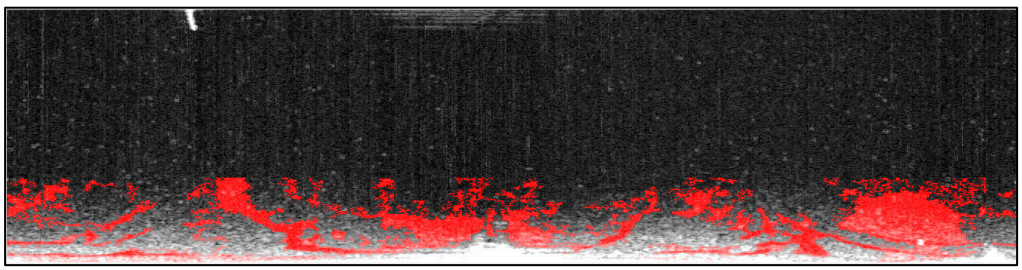

Figure 6. Oil film segmentation result with traditional MBO algorithm.

4.2. Comparison Between Improved MBO Algorithm and Other Optimization Algorithms

The performance advantage of the improved MBO algorithm in oil spill region segmentation was further evaluated by comparison with the Ant Colony Optimization (ACO), the PSO, and the Simulated Annealing Optimization (SAO) [38–40]. The aforementioned algorithms were applied to the oil spill ROI extraction images for comparative analysis, and the results are presented in Figure 7. The ACO algorithm effectively identified oil spill regions, whereas pronounced misclassification of background areas was also observed. Such misclassification introduced spurious targets, degrading segmentation accuracy, consequently impairing segmentation efficiency and overall detection performance. The PSO

algorithm detected certain oil spill regions, yet its vulnerability to noise and complex background textures frequently resulted in the misclassification of non-oil areas. The SAO algorithm enabled the identification of partial oil spill regions and demonstrated effective control over false detections. Nevertheless, detection completeness for actual oil spill regions remained limited, with pronounced missed detections constraining overall accuracy in practical applications.

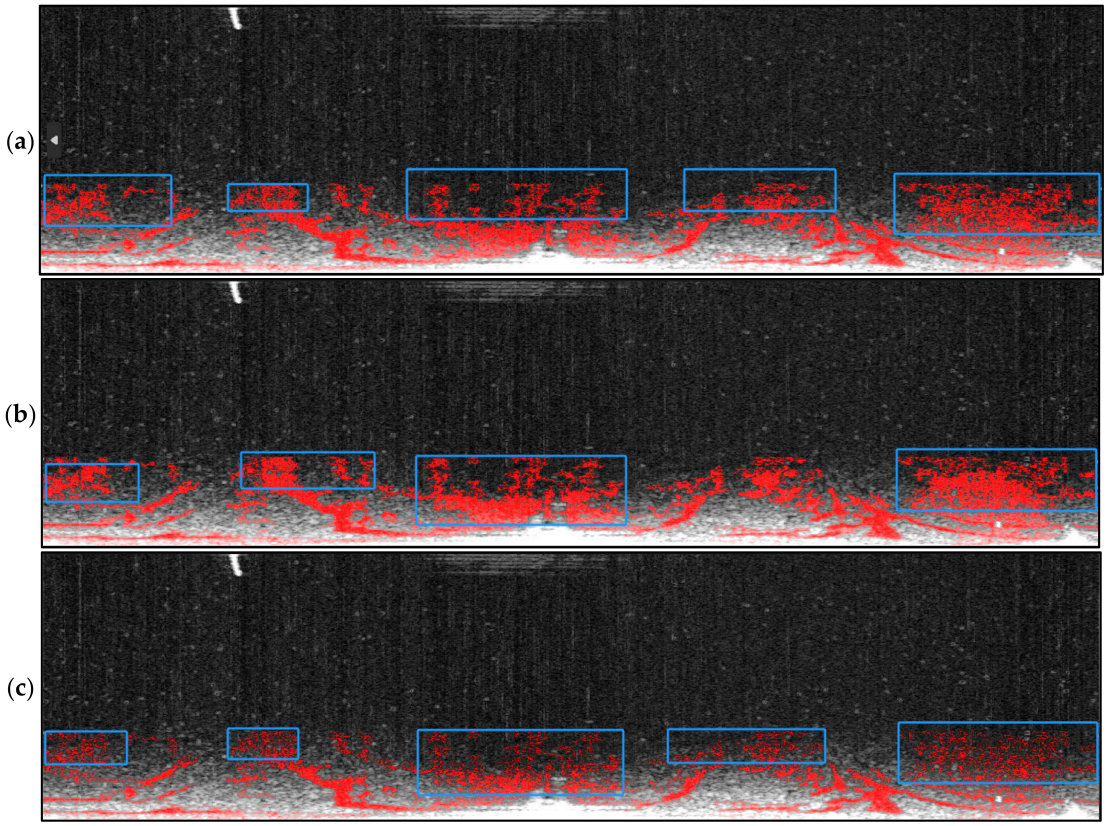

Figure 7. Oil film segmentation with different algorithms: (**a**) ACO, (**b**) PSO, and (**c**) SAO. The blue box indicates the misclassified region.

4.3. Different Networks and Classifiers Extracted ROI Images

A standalone RBF network, SVM classifier and RF classifier were introduced to improve the completeness of the comparative experiments for ROI image extraction. The experimental results indicated that the standard RBF neural network, due to its reliance on manually preset core parameters, could not adaptively capture pixel features across the entire image. This limitation reduced the feature separability between target and background regions and significantly increased classification fitting errors. Consequently, the resulting ROI extraction visually exhibited clear discontinuities and fragmentation, as shown in Figure 8a. The results generated by the RF method contained substantial noise and numerous scattered artifacts. Large areas of false detections were also observed, causing the ROI image to exhibit significant fragmentation and poor spatial continuity, as shown in Figure 8b. Although the SVM method was able to extract part of the oil spill features effectively, a considerable amount of noise was still present in the extraction results. The extracted regions exhibited highly scattered distribution characteristics, and a large number of background pixels were falsely identified as ROI regions, as shown in Figure 8c.

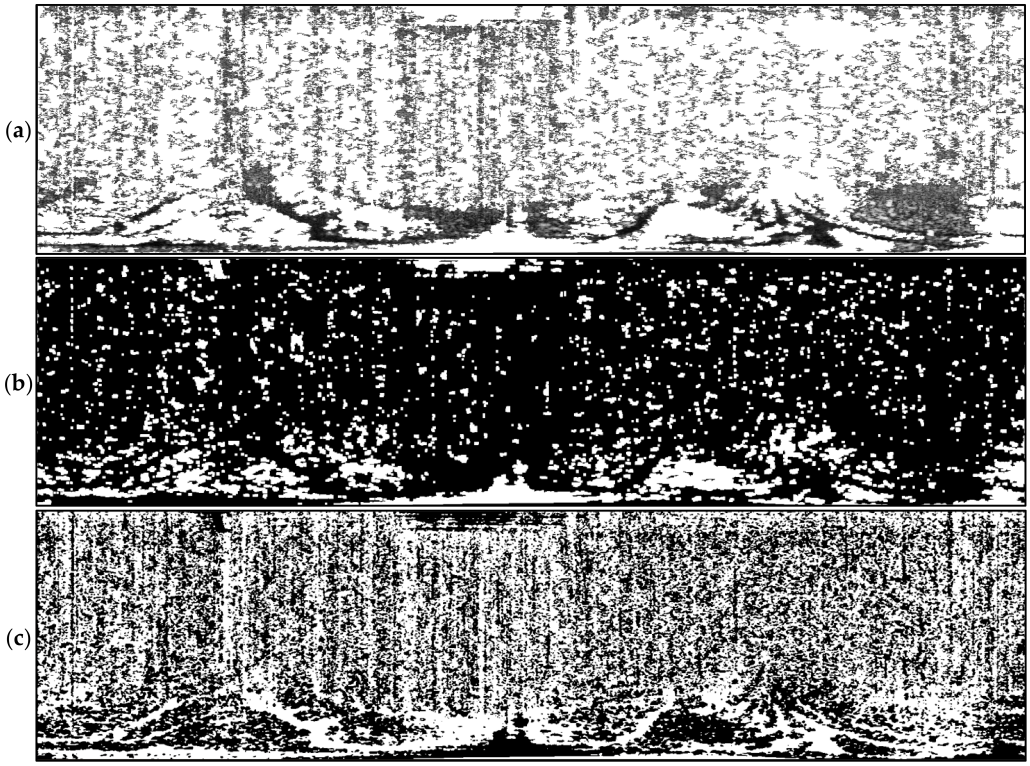

Figure 8. ROI image extraction results. (**a**) RBF neural network, (**b**) RF classifier, and (**c**) SVM classifier.

4.4. Comparison of Different Threshold Segmentation Methods

The preprocessed images were segmented by using the Otsu, Phansalkar, and Sauvola thresholding methods while all other parameters remained consistent [41–43], as shown in Figure 9. The Otsu thresholding method detected most of the oil film regions, but it showed limited precision at the edges. This limitation frequently caused the oil film boundaries to merge with the background, resulting in the expansion of oil film areas and misclassification of surrounding regions. The Phansalkar algorithm enabled a coarse delineation of the primary oil film extent, yet the extracted boundaries were markedly irregular and highly fragmented. This led to evident adhesion and false merging between oil film edges and the sea surface background, compromising morphological continuity and hindering accurate representation of the true diffusion boundary. The oil film patches detected by the Sauvola algorithm exhibited pronounced jagged and discontinuous boundaries, thereby creating ambiguous transitions between the oil film and the background. This ambiguity facilitated the misclassification of surrounding dark clutter as oil spill regions, leading to unreasonable expansion of the detected spill extent.

4.5. Comparison with Deep Learning Networks

The effectiveness of the proposed MBO framework was further evaluated by comparison with two representative deep learning segmentation architectures, U-Net and DeepLabV3+. As representative semantic segmentation architectures, these models provided effective benchmark references for evaluating optimization performance in limited training sample scenarios.

Given the limited number of manually annotated radar images, a patch-based training strategy was employed to increase the effective number of training samples and enhance the feature learning capability of the model for oil spill regions. Precision, Recall, F1-score, and IoU were uniformly adopted as evaluation metrics to maintain consistency and fairness in the comparative analysis. The experimental results indicated that U-Net and DeepLabV3+ retained the ability to perform basic oil spill segmentation and preserve major target struc-

tures under limited-sample conditions. However, the limited training data restricted their discriminative capability in complex textured regions, thereby causing blurred boundaries and the omission of small targets, which ultimately degraded the overall segmentation performance, as shown in Figure 10. In contrast, the proposed MBO framework delivered more stable segmentation performance, thereby demonstrating the robustness and practical applicability of optimization-based methods in limited-sample scenarios.

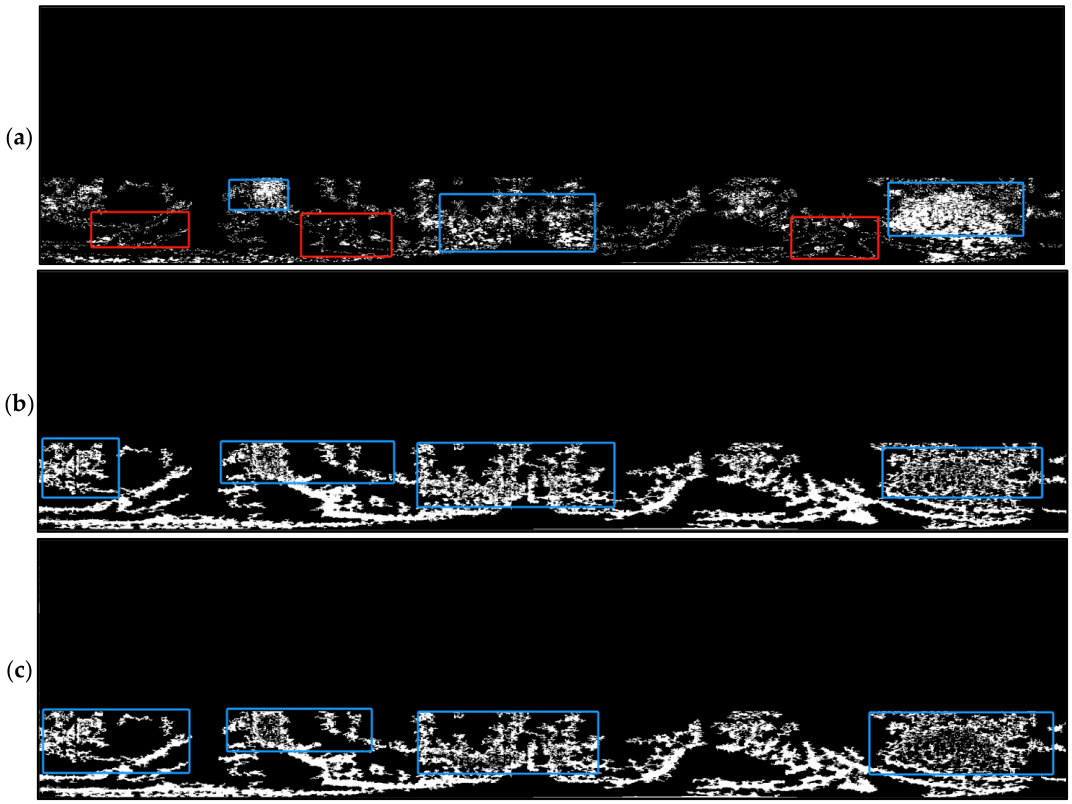

Figure 9. Segmentation results of different adaptive threshold algorithms: (**a**) Otsu threshold segmentation, (**b**) Phansalkar threshold segmentation, and (**c**) Sauvola threshold segmentation. The blue box indicates the misclassified region. The red box indicates the undetected region.

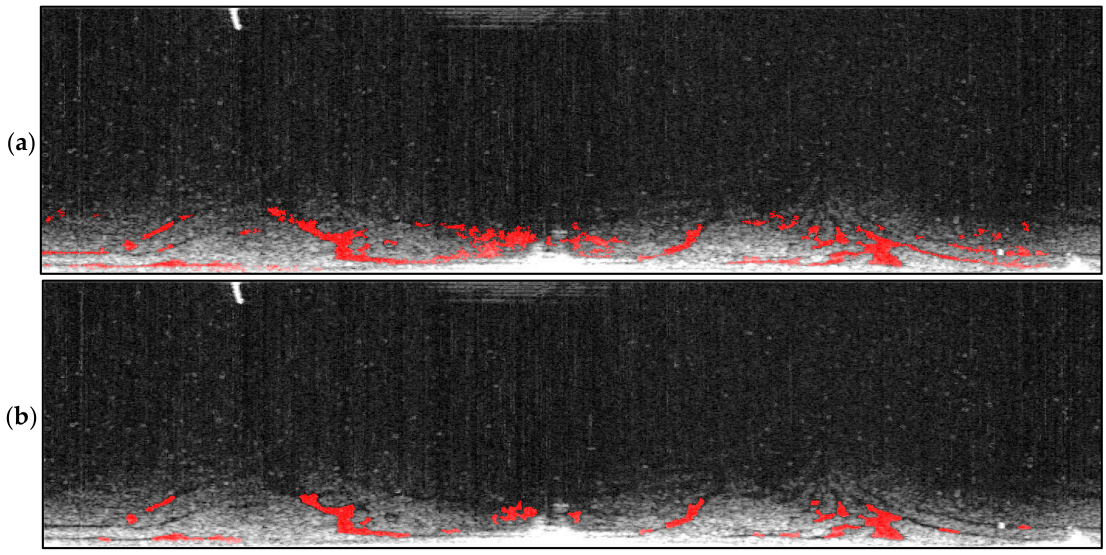

Figure 10. Deep Learning-Based Oil Spill Segmentation Results. (**a**) U-net and (**b**) DeeplabV3.

The improved MBO framework achieved reliable extraction of oil spill regions in radar imagery, while the deep learning models exhibited misclassification in low-contrast and small-area oil spill regions, mainly due to the insufficient amount of training data. Overall, the proposed MBO method maintained stable segmentation performance under limited annotated data conditions, thereby confirming its practical value in marine oil spill monitoring applications.

4.6. Visual Interpretation and Quantitative Analysis

The superiority of the improved MBO algorithm in oil spill region extraction was intuitively validated by introducing a manual visual interpretation method for comparative analysis, as shown in Figure 11a. The green areas in the figure represent true positive regions, corresponding to the real oil spill areas accurately identified by both the algorithm and manual interpretation. The red areas indicate false positive regions, where the algorithm misidentified oil spills while manual interpretation confirmed the absence of actual oil films. The blue areas represent false negative regions, corresponding to areas where actual oil films were present but were not effectively detected by the algorithm. During manual visual interpretation, the boundaries of oil film regions must be manually delineated, as revealed by a systematic analysis of multiple oil spill experimental samples. However, visual interpretation exhibits significant limitations and subjective judgment variability. These issues inevitably lead to deviations in oil film boundary localization and contour distortion, thereby affecting the accuracy and consistency of interpretation results. Compared with the inherent limitations of manual visual interpretation, the proposed optimized algorithm operated without human intervention.

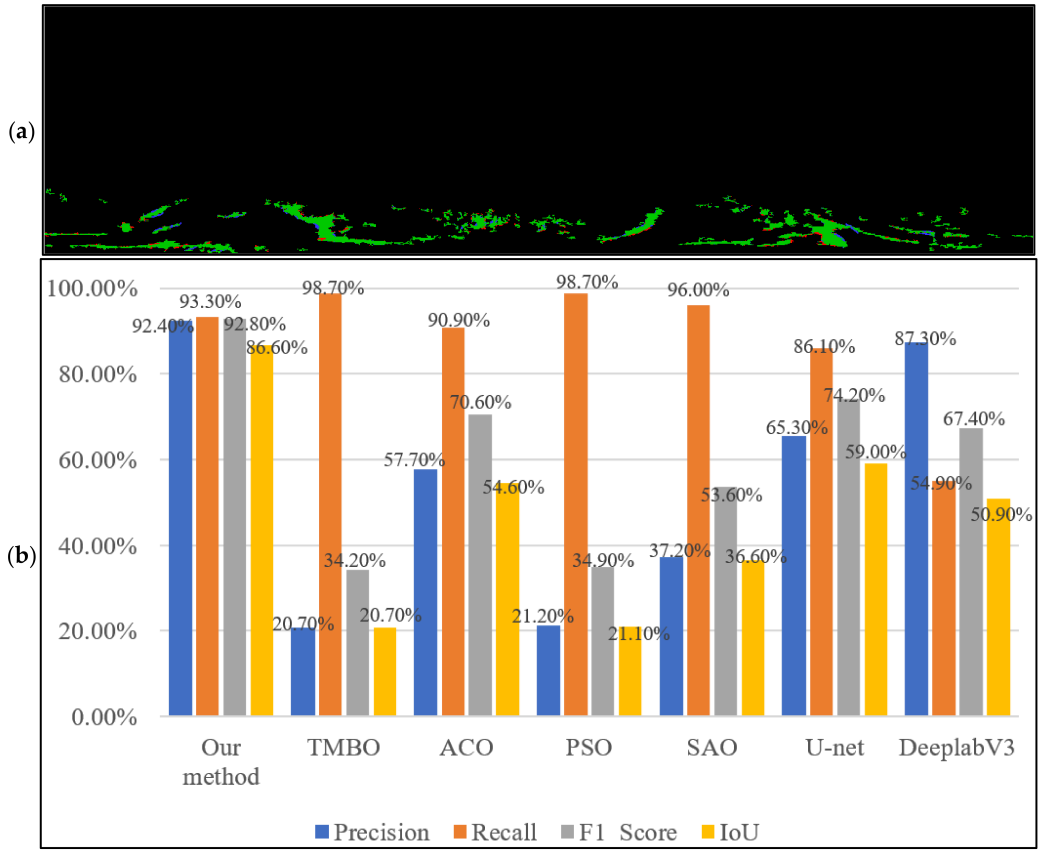

Figure 11. Visual interpretation analysis result: (**a**) Interpretation and analysis results of the improved MBO algorithm, and (**b**) Comparative results of performance metrics.

The quantitative evaluation results demonstrate that the improved MBO algorithm achieves the best overall segmentation performance among all comparison methods. Specifically, the Precision, Recall, F1-score, and IoU values reached 92.4%, 93.3%, 92.8%, and 86.6%, respectively, as shown in Table 1. The comparative evaluation between the improved MBO algorithm and alternative optimization methods was conducted, with the resulting performance metrics illustrated in Figure 11b. Although TMBO, DeepLabV3 and U-Net obtained slightly higher Recall values, their F1 score and IoU values were significantly lower, suggesting the presence of severe over-segmentation and excessive false-positive regions. This indicates that a high Recall value alone cannot comprehensively reflect segmentation quality. In contrast, the improved MBO algorithm achieves a more balanced trade-off between Precision and Recall, thereby providing more accurate oil spill region extraction and boundary delineation.

Table 1. Improvement analysis of the proposed MBO algorithm compared with the second-best method.

Metric	Second-Best Method	Second-Best Value (%)	Our Method (%)	Absolute Gain	Relative Improvement (%)
Precision	DeepLabV3	87.30	92.40	5.10	5.84
Recall	TMBO	98.70	93.30	−5.40	−5.47
F1 score	U-Net	74.20	92.80	18.60	25.07
loU	U-Net	59.00	86.60	27.60	46.78

4.7. Ablation Experiment

Ablation experiments were performed to evaluate the necessity of the key strategies in the improved MBO algorithm. Four enhancement modules were investigated, including elite reproduction, opposition-based learning, dynamic parameter adjustment, and the multi-objective fitness function. Identical datasets and evaluation metrics were maintained throughout all experiments.

The ablation experimental results demonstrated that different improvement strategies influenced the algorithm performance from multiple aspects. The dynamic parameter adjustment mechanism adaptively balanced global exploration and local exploitation during the iterative process, thereby improving the stability and efficiency of convergence. The opposition-based learning strategy expanded the population distribution by introducing opposite solutions, thereby enhancing the coverage capability of the search space. The elite reproduction mechanism preserved and reused high-quality individuals, which prevented the optimal solution from being disrupted by random perturbations during iteration. The multi-objective fitness function combined multiple evaluation criteria, enabling the optimization process to simultaneously preserve region integrity and enhance boundary delineation accuracy. Each component played a critical role in the optimization process. The removal of any module led to a noticeable degradation in overall performance, making it difficult to obtain superior optimization results. Different experimental groups were established by progressively introducing elite reproduction, opposition-based learning, dynamic parameter adaptation, and the multi-objective fitness function. Quantitative comparisons among these groups were performed to evaluate the contribution of each strategy and the overall enhancement achieved by the integrated optimization framework. The corresponding visual comparison results are presented in Figure 12, and the quantitative evaluation metrics are summarized in Table 2.

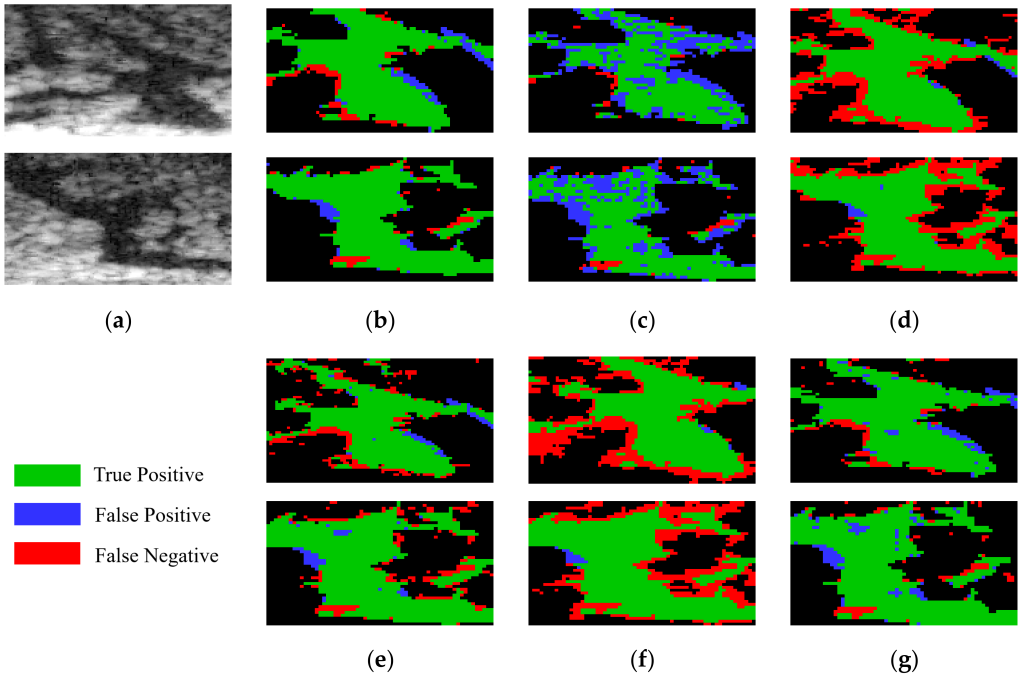

Figure 12. Ablation experiment results. (**a**) Marine radar image, (**b**) Our method, (**c**) Elite reproduction, (**d**) Opposition-based learning, (**e**) Dynamic parameters, (**f**) Multi-objective fitness function, and (**g**) Individual multi-objective fitness function.

Table 2. Quantitative analysis results of Ablation Experiment.

Elite Reproduction	Opposition-Based Learning	Dynamic Parameters	Multi-Objective Fitness Function	Precision (%)	Recall (%)	F1 Score (%)	IoU (%)
√	√	√	√	92.4	93.3	92.8	86.6
	√	√	√	75.4	56.9	64.8	48.0
√		√	√	23.1	98.4	37.4	23.0
√	√		√	49.2	93.3	64.4	47.5
√	√	√		22.0	98.6	35.9	21.9
			√	61.0	89.8	72.7	57.1

The results indicate that the traditional MBO algorithm achieved relatively lower segmentation accuracy and boundary completeness. After introducing the proposed improvement strategies, the segmentation performance was progressively enhanced in terms of Precision, F1-score, and IoU. The improved MBO framework achieved the best overall segmentation performance, demonstrating the complementary effectiveness of the proposed modification strategies.

5. Conclusions

Oil film extraction from marine radar images was conducted using a GA-RBF neural network combined with the improved MBO algorithm. The proposed framework effectively enhanced the discrimination capability between oil spill regions and surrounding clutter while improving segmentation completeness. The introduced adaptive parameter adjustment, opposition-based learning, elite-guided reproduction, and multi-dimensional weighted fitness function jointly enhanced optimization stability, population diversity, and segmentation discrimination capability. The proposed method is developed based on an unsupervised optimization framework, thereby reducing dependence on large-scale annotated samples and enabling adaptive oil spill detection under different marine scene conditions. Extension of the proposed framework to multi-scene and large-scale datasets

can facilitate broader validation of its robustness and applicability under complex marine environments. Compared with traditional optimization algorithms, the proposed method achieved more accurate extraction of oil spill regions and more stable segmentation performance under complex marine radar conditions. Although the method demonstrated good performance in oil spill extraction tasks, certain limitations still existed. Although the experiments were conducted on a limited dataset, the unsupervised nature of the proposed method reduces its dependence on large-scale annotated samples and enables adaptive detection under different marine scene conditions. Based on this characteristic, the proposed method will be extended to multi-scene and large-scale datasets to investigate its robustness and practical applicability in more complex marine environments.

The ability of the algorithm to distinguish oil film boundaries under complex clutter conditions needs to be improved. In particular, when high sea states and strong wind conditions are present, the radar backscatter characteristics of oil spill regions become increasingly similar to those of the surrounding sea surface. This phenomenon weakens the inter-class separability between oil spills and background clutter, thereby reducing the discrimination capability of the multi-objective fitness function. In addition, adaptability under different illumination conditions and sea states needs to be further considered, thereby optimizing the overall computational efficiency. The study was conducted on a single dataset, and the number of samples remained relatively limited. The limitation of a single dataset lies in its insufficient coverage of diverse sea states, regions, and environmental conditions, which may lead the model to learn localized features specific to particular scenarios. Moreover, the limited sample size was insufficient to support stable training and reliable generalization validation of deep learning models, thereby restricting model generalization ability and robustness to some extent.

Future work will focus on constructing a more diverse oil spill radar dataset. This dataset will incorporate varying sea state conditions, complex ocean surface environments, and multi-regional observational data. These efforts will improve the comprehensiveness and reliability of model evaluation and further enhance model generalization capability and practical applicability. In addition, the adaptive parameter adjustment mechanism will be further optimized to enhance algorithm robustness and adaptability. A multidimensional environmental feature adaptation module will be introduced. The robustness of the algorithm in complex marine interference environments will be improved. The practicality and generalization ability of the algorithm will be further enhanced. This will provide more efficient and reliable technical support for precise marine oil spill monitoring.

Author Contributions: Conceptualization, J.X. and B.X.; methodology, B.X.; software, B.X. and J.X.; validation, B.Y., Z.G. and M.Y.; resources, J.Y.; data curation, J.Y. and L.Q.; writing—original draft preparation, B.X.; writing—review and editing, J.X. and B.X.; supervision, J.X. and P.L.; project administration, J.X.; funding acquisition, J.X., J.Y. and L.Q. All authors have read and agreed to the published version of the manuscript.

Funding: This research was supported the Guangdong Basic and Applied Basic Research Foundation, grant numbers 2025A1515010886, 2023A1515011212, National Natural Science Foundation of China, grant number 52271359, the Special Projects in Key Fields of Ordinary Universities in Guangdong Province, grant number 2022ZDZX3005, the Shenzhen Science and Technology Program, grant number JCYJ20220530162200001, Postgraduate Education Innovation Project of Guangdong Ocean University, grant numbers 202421, 202539, 202551, the Guangdong Provincial Key Laboratory of Intelligent Equipment for South China Sea Marine Ranching, grant number 2023B1212030003, the Research Project of Higher Education Institutions in Anhui Province, China, grant number 2024AH051743.

Data Availability Statement: The copyright for the data application is owned by Dalian Maritime University. Any inquiries should be directed to Dalian Maritime University.

Conflicts of Interest: The authors declare no conflicts of interest.

References

1. Liu, P.; Zhao, Y.; Liu, B.; Li, Y.; Chen, P. Oil spill extraction from X-band marine radar images by power fitting of radar echoes. *Remote Sens. Lett.* **2021**, *12*, 345–352. [CrossRef]
2. Guo, S.; Li, Y.; Shang, J.; Cheng, L. GSSNet: Gated selective scan network for port oil spill pollution detection. *Measurement* **2025**, *256*, 118086. [CrossRef]
3. Deng, Y.; Yao, B.; Xu, J.; Qiao, L.; Chen, B.; Sun, M. Oil spill detection method for marine radar based on multi-dimensional features and improved MShOA. *Mar. Environ. Sci.* **2026**, *45*, 417–423. [CrossRef]
4. Nukapothula, S.; Suneel, V.; Yunus, A.P.; Rao, V.T.; Chen, C. Impact assessment of oil spills on the Red Sea waters using remote sensing and numerical modeling. *Reg. Stud. Mar. Sci.* **2025**, *86*, 104187. [CrossRef]
5. Wang, L.; Lu, Y.; Wang, M.; Zhao, W.; Lv, H.; Song, S.; Wang, Y.; Chen, Y.; Zhan, W.; Ju, W. Mapping of oil spills in China Seas using optical satellite data and deep learning. *J. Hazard. Mater.* **2024**, *480*, 135809. [CrossRef]
6. Cui, G.; Fan, J.; Zou, Y. Enhanced unsupervised domain adaptation with iterative pseudo-label refinement for inter-event oil spill segmentation in SAR images. *Int. J. Appl. Earth Obs. Geoinf.* **2025**, *139*, 104479. [CrossRef]
7. Rajendran, S.; Vethamony, P.; Sadooni, F.N.; Al-Kuwari, H.A.-S.; Al-Khayat, J.A.; Seegobin, V.O.; Govil, H.; Nasir, S. Detection of Wakashio oil spill off Mauritius using Sentinel-1 and 2 data: Capability of sensors, image transformation methods and mapping. *Environ. Pollut.* **2021**, *274*, 116618. [CrossRef]
8. Li, G.; Lv, G.; Li, B.; Wang, X.; Zhao, F. Performance of Oil Spill Identification in Multiple Scenarios Using Quad-, Compact-, and Dual-Polarization Modes. *J. Mar. Sci. Eng.* **2026**, *14*, 113. [CrossRef]
9. Yuan, L.; Xie, B.; Cui, Y.; Zhang, X.; Jiao, H. Research on oil spill status recognition based on LIF. *Spectrosc. Spectr. Anal.* **2022**, *42*, 2018–2024. [CrossRef]
10. Liu, T.; Cao, R.; Zhang, M.; Chen, X.; Bi, F.; Xu, J. Oil Spill Occurrence and Pollution Risk Assessment Based on Sea State, Oil Platform Location, and Shipping Route Density in the Bohai Sea. *J. Mar. Sci. Eng.* **2025**, *13*, 729. [CrossRef]
11. Chen, R.; Jia, B.; Ma, L.; Xu, J.; Li, B.; Wang, H. Marine radar oil spill extraction based on texture features and BP neural network. *J. Mar. Sci. Eng.* **2022**, *10*, 1904. [CrossRef]
12. Cheng, L.; Li, Y.; Zhang, X.; Xie, M. An Analysis of the optimal features for Sentinel-1 oil spill datasets based on an improved J–M/K-means algorithm. *Remote Sens.* **2022**, *14*, 4290. [CrossRef]
13. Xu, J.; Cheng, M.; Li, B.; Chu, L.; Dong, H.; Yang, Y.; Qian, S.; Huang, Y.; Yuan, J. Oil Slick Identification in Marine Radar Image Using HOG, Random Forest, and PSO. *IEEE Geosci. Remote Sens. Lett.* **2024**, *21*, 1504305. [CrossRef]
14. Li, K.; Yu, H.; Xu, Y.; Luo, X. Detection of oil spills based on gray level co-occurrence matrix and support vector machine. *Front. Environ. Sci.* **2022**, *10*, 1049880. [CrossRef]
15. Ma, X.; Xu, J.; Wu, P.; Kong, P. Oil spill detection based on deep convolutional neural networks using polarimetric scattering information from Sentinel-1 SAR images. *IEEE Trans. Geosci. Remote Sens.* **2021**, *60*, 4204713. [CrossRef]
16. Prajapati, K.; Bhavsar, M.; Mahajan, A. GSCAT-UNET: Enhanced U-Net model with spatial-channel attention gate and three-level attention for oil spill detection using SAR data. *Mar. Pollut. Bull.* **2025**, *212*, 117583. [CrossRef] [PubMed]
17. Sun, C.; Wang, D.; Xu, M.; Wei, S.; Liu, S.; Li, Z. MAF-UFormer: Oil Spill Detection in SAR Images Using Multi-scale Alignment and Fusion U-Shaped Transformer Network. *Reg. Stud. Mar. Sci.* **2026**, *94*, 104773. [CrossRef]
18. Bianchi, F.M.; Espeseth, M.M.; Borch, N. Large-scale detection and categorization of oil spills from SAR images with deep learning. *Remote Sens.* **2020**, *12*, 2260. [CrossRef]
19. Cai, Y.; Chen, L.; Zhuang, X.; Zhang, B. Automated marine oil spill detection algorithm based on single-image generative adversarial network and YOLO-v8 under small samples. *Mar. Pollut. Bull.* **2024**, *203*, 116475. [CrossRef] [PubMed]
20. Zhang, J.; Yang, P.; Ren, X. Detection of oil spill in SAR image using an improved DeepLabV3+. *Sensors* **2024**, *24*, 5460. [CrossRef]
21. Lau, T.-K.; Huang, K.-H. A timely and accurate approach to nearshore oil spill monitoring using deep learning and GIS. *Sci. Total. Environ.* **2024**, *912*, 169500. [CrossRef]
22. Wang, Y.; Wang, L.; Chen, X.; Liang, D. Offshore petroleum leaking source detection method from remote sensing data via deep reinforcement learning with knowledge transfer. *IEEE J. Sel. Top. Appl. Earth Obs. Remote Sens.* **2022**, *15*, 5826–5840. [CrossRef]
23. Li, C.; Kim, D.-J.; Park, S.; Kim, J.; Song, J. A self-evolving deep learning algorithm for automatic oil spill detection in Sentinel-1 SAR images. *Remote Sens. Environ.* **2023**, *299*, 113872. [CrossRef]
24. Yuan, Y.-M.; Xiong, W.; Fang, Y.-H.; Lan, T.-G.; Li, D.-C. Detection of oil spills on water by differential polarization FTIR spectrometry. *Spectrosc. Spectr. Anal.* **2010**, *30*, 2129–2132. [CrossRef]
25. Iordache, M.-D.; Viallefont-Robinet, F.; Strackx, G.; Landuyt, L.; Moelans, R.; Nuyts, D.; Vandeperre, J.; Knaeps, E. Feasibility of Oil Spill Detection in Port Environments Based on UV Imagery. *Sensors* **2025**, *25*, 1927. [CrossRef]
26. Chen, Y.; Wang, Z. Marine oil spill detection from SAR images based on attention U-Net model using polarimetric and wind speed information. *Int. J. Environ. Res. Public Health* **2022**, *19*, 12315. [CrossRef] [PubMed]

27. Liu, P.; Li, Y.; Xu, J.; Wang, T. Oil spill extraction by X-band marine radar using texture analysis and adaptive thresholding. *Remote Sens. Lett.* **2019**, *10*, 583–589. [CrossRef]
28. Rousso, R.; Katz, N.; Sharon, G.; Glizerin, Y.; Kosman, E.; Shuster, A. Automatic recognition of oil spills using neural networks and classic image processing. *Water* **2022**, *14*, 1127. [CrossRef]
29. Karantzalos, K.; Argialas, D. Automatic detection and tracking of oil spills in SAR imagery with level set segmentation. *Int. J. Remote Sens.* **2008**, *29*, 6281–6296. [CrossRef]
30. Liu, S.; Chi, M.; Zou, Y.; Samat, A.; Benediktsson, J.A.; Plaza, A. Oil spill detection via multitemporal optical remote sensing images: A change detection perspective. *IEEE Geosci. Remote Sens. Lett.* **2017**, *14*, 324–328. [CrossRef]
31. Lyu, X.; Han, H.; Ren, P.; Grecos, C. DiffusionLSTM: A framework for image sequence generation and its application to oil spill monitoring and prediction. *IEEE Trans. Geosci. Remote Sens.* **2024**, *62*, 5632313. [CrossRef]
32. Tan, L.; Zhao, R.; Yin, X.; Zhang, H.; Wang, J. Establishment and application of an intelligent treating method for oil spill identification. *Acta Oceanol. Sin.* **2018**, *37*, 116–122. [CrossRef]
33. Yan, C.; Li, M.-X.; Liu, W. Application of Improved Genetic Algorithm in Function Optimization. *J. Inf. Sci. Eng.* **2019**, *35*, 6. [CrossRef]
34. Jiang, Q.; Zhu, L.; Shu, C.; Sekar, V. An efficient multilayer RBF neural network and its application to regression problems. *Neural Comput. Appl.* **2021**, *34*, 4133–4150. [CrossRef]
35. El-Shorbagy, M.A.; Alhadbani, T.H. Monarch butterfly optimization-based genetic algorithm operators for nonlinear constrained optimization and design of engineering problems. *J. Comput. Des. Eng.* **2024**, *11*, 200–222. [CrossRef]
36. Feng, Y.; Yu, X.; Wang, G.-G. A novel monarch butterfly optimization with global position updating operator for large-scale 0-1 knapsack problems. *Mathematics* **2019**, *7*, 1056. [CrossRef]
37. Wang, G.-G.; Deb, S.; Cui, Z. Monarch butterfly optimization. *Neural Comput. Appl.* **2015**, *31*, 1995–2014. [CrossRef]
38. Yu, L.; Lian, J.; Li, Y.; Du, Y.; Wang, D. An Enhanced Ant Colony Optimization for Path Planning of a Mobile Robot. *Optim. Control Appl. Methods* **2025**, *47*, 387–398. [CrossRef]
39. Jiang, J.-J.; Wei, W.-X.; Shao, W.-L.; Liang, Y.-F.; Qu, Y.-Y. Research on large-scale bi-level particle swarm optimization algorithm. *IEEE Access* **2021**, *9*, 56364–56375. [CrossRef]
40. Geng, X.; Xu, J.; Xiao, J.; Pan, L. A simple simulated annealing algorithm for the maximum clique problem. *Inf. Sci.* **2007**, *177*, 5064–5071. [CrossRef]
41. Xu, X.; Xu, S.; Jin, L.; Song, E. Characteristic analysis of Otsu threshold and its applications. *Pattern Recognit. Lett.* **2011**, *32*, 956–961. [CrossRef]
42. Zhang, Y.; Qin, J.; Han, J.; Xie, G. Design of a stochastic computing architecture for the phansalkar algorithm. *IEEE Trans. Very Large Scale Integr. Syst.* **2024**, *32*, 442–454. [CrossRef]
43. Liu, P.; Wang, X.; Shao, P.; Zhao, X.; Liu, B.; Chen, P.; Zhu, X.; Xu, J.; Li, Y. Oil spill segmentation in marine radar images based on the improved Sauvola algorithm. *Remote Sens. Lett.* **2026**, *17*, 182–189. [CrossRef]

Disclaimer/Publisher's Note: The statements, opinions and data contained in all publications are solely those of the individual author(s) and contributor(s) and not of MDPI and/or the editor(s). MDPI and/or the editor(s) disclaim responsibility for any injury to people or property resulting from any ideas, methods, instructions or products referred to in the content.